CHEMISTRY OF MATERIALS

pubs.acs.org/cm Article

Ubiquitous Near-Band-Edge Defect State in Rare-Earth-Doped Lead-Halide Perovskites

Tyler J. Milstein, Joo Yeon D. Roh, Laura M. Jacoby, Matthew J. Crane, David E. Sommer, Scott T. Dunham, and Daniel R. Gamelin*

Cite This: https://doi.org/10.1021/acs.chemmater.2c00132 Read Online

ABSTRACT: $CsPb(Cl_{1-x}Br_x)_3$ ($0 \leq x \leq 1$) nanocrystals and thin films doped with a series of trivalent rare-earth ions (RE^{3+} = Y^{3+}, La^{3+}, Ce^{3+}, Gd^{3+}, Er^{3+}, Lu^{3+}) have been prepared and studied using variable-temperature and time-resolved photoluminescence spectroscopies. We demonstrate that aliovalent (trivalent) doping of this type universally generates a new and often-emissive defect state ca. 50 meV inside the perovskite band gap, independent of the specific RE^{3+} dopant identity or of the perovskite form (nanocrystals vs thin films). Chloride-to-bromide anion exchange is used to demonstrate that this near-band-edge photoluminescence shifts with changing band-gap energy to remain just below the excitonic luminescence for all compositions of $CsPb(Cl_{1-x}Br_x)_3$ ($0 \leq x \leq 1$). Computations show that this shift stems from the effect of the changing lattice dielectric constants on a shallow defect-bound exciton. Microscopic descriptions of this dopant-induced near-band-edge state and its relation to quantum cutting in Yb^{3+}-doped $CsPb(Cl_{1-x}Br_x)_3$ are discussed.

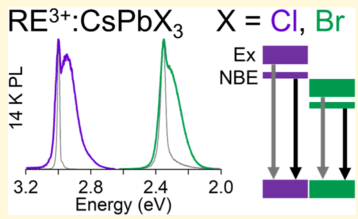

■ INTRODUCTION

Trivalent rare-earth (RE^{3+}) doping of all-inorganic lead-halide perovskites ($CsPbX_3$, X = halide) has recently attracted broad interest. In $CsPbI_3$, Eu^{3+} and Yb^{3+} dopants have been found to enhance the stability of the desired α-phase and to yield superior photovoltaic efficiencies compared to their undoped counterparts.[1,2] Another study reported enhancement of the power conversion efficiencies (PCEs) from 7% in solar cells based on undoped $CsPbBr_3$ to ~10% in cells using RE^{3+}-doped $CsPbBr_3$ (RE^{3+}:$CsPbBr_3$, where RE^{3+} = Sm^{3+}, Tb^{3+}, Ho^{3+}, Er^{3+}, Yb^{3+}).[3] RE^{3+} doping has also been reported to enhance excitonic photoluminescence quantum yields (PLQYs), even for RE^{3+} ions that are spectroscopically innocent (i.e., lacking electronic transitions of their own within the perovskite energy gap), such as Y^{3+},[4] La^{3+},[4] Ce^{3+},[5,6] Gd^{3+},[7] and Lu^{3+}.[4] Other RE^{3+} dopants that do have internal electronic excited states at midgap energies have been used to generate new near-infrared (NIR) and/or visible emission from lead-halide perovskites through PL sensitization.[8−10]

Particularly notable is the observation of PLQYs exceeding 100% in Yb^{3+}:$CsPb(Cl_{1-x}Br_x)_3$ perovskites.[8,10−28] This phenomenon occurs via "quantum cutting", in which absorption of a high-energy photon generates emission of two Yb^{3+} $^2F_{5/2} \rightarrow {}^2F_{7/2}$ photons in the NIR, each at ca. half the absorbed photon's energy. It has been hypothesized[13] that quantum cutting in Yb^{3+}:$CsPb(Cl_{1-x}Br_x)_3$ is facilitated by a defect state associated with charge compensation of the aliovalent Yb^{3+} dopants. Transient-absorption measurements have demonstrated perovskite exciton-bleach recovery on the timescale as short as a few picoseconds upon Yb^{3+} doping,[13] but Yb^{3+} PL shows a rise time of ~8 ns,[23] supporting the participation of an intermediate state in this quantum-cutting mechanism. The strong PLQY dependence on the $CsPbX_3$ energy gap in the region of $E_g \sim 2 \times E_{f-f}$ further suggests that this intermediate state must be close in energy to the exciton.[19] An interesting related hypothesis is that the quantum-cutting intermediate state involves the capture of a photogenerated conduction-band electron by an individual Yb^{3+} ion to form Yb^{2+}, which subsequently relaxes to excite two Yb^{3+} ions to their $^2F_{5/2}$ excited states.[24,28] One approach to refine the above hypotheses experimentally is to examine the photophysical effects of spectroscopically innocent RE^{3+} dopants in $CsPbX_3$ perovskites. Despite numerous studies of RE^{3+}:$CsPbX_3$ aimed at applications, the more general effects of aliovalent RE^{3+} doping in lead−halide perovskites are not yet well characterized. Such fundamental studies will improve the understanding of aliovalent doping in these materials and of the ensuing photophysical consequences.

To this end, we report here an investigation of the low- and variable-temperature (VT) PL of a series of RE^{3+}:$CsPb(Cl_{1-x}Br_x)_3$ nanocrystals (NCs) and thin films to understand the effects of RE^{3+} dopants on the perovskite electronic structure and photophysics. To ensure that we are only probing structural and electrostatic effects, we focus primarily on RE^{3+} dopants that have no interfering f−f, d−d, f−d, or

Received: January 14, 2022
Revised: March 29, 2022

charge-transfer transitions within the perovskite energy gap (Y^{3+}, La^{3+}, Ce^{3+}, Gd^{3+}, and Lu^{3+}). These experiments reveal that *all* of these spectroscopically innocent RE^{3+} dopants give rise to similar near-band-edge (NBE) PL at low temperatures, characterized by a binding energy of ~50 meV. Intense NBE PL is observed for $0 \leq x \leq 1$, with a binding energy that decreases slightly upon converting from RE^{3+}:$CsPbCl_3$ to RE^{3+}:$CsPbBr_3$, attributable to the increasing dielectric constants of the perovskite lattice across this series. The NBE PL also shows a strong temperature dependence that suppresses most intensity above ~100 K, but it is still clearly manifested in time-resolved PL (TRPL) measurements at room temperature, indicating that this state remains influential. The study is further extended to Er^{3+}:$CsPb(Cl_{1-x}Br_x)_3$, which also displays the same NBE PL at low temperature despite having internal *f*–*f* excited states within the perovskite energy gap. The RE^{3+} dopants examined here thus span the full range of lanthanide atomic numbers and include the nonlanthanide, Y^{3+}. Consequently, we conclude that *all* such trivalent substitutional dopants will generate the same NBE defect state in $CsPbX_3$ perovskites. These results have interesting ramifications for the interpretation of doping effects on both the photophysical and electronic properties of lead-halide perovskites, and they inform the development of doped perovskites for future optoelectronic technologies.

EXPERIMENTAL SECTION

Materials. 1-Octadecene (ODE, 90%, Sigma-Aldrich), oleylamine (OAm, 70%, Sigma-Aldrich), oleic acid (OA, 90%, Sigma-Aldrich), *n*-hexane (99%, Sigma-Aldrich), ethyl acetate (EtOAc, 99%, Sigma-Aldrich), ethanol (EtOH, 200 proof, Decon Laboratories, Inc.), trimethylsilyl chloride (TMS-Cl, 98%, Acros Organics), trimethylsilyl bromide (TMS-Br, 97%, Sigma-Aldrich), lead(II) acetate trihydrate (99.999%, $Pb(OAc)_2 \cdot 3H_2O$, Sigma-Aldrich), cesium acetate (CsOAc, 99.9%, Sigma-Aldrich), yttrium(III) acetate hydrate (99.9%, $Y(OAc)_3 \cdot xH_2O$, Sigma-Aldrich), lanthanum(III) acetate hydrate (99.9%, $La(OAc)_3 \cdot xH_2O$, Strem Chemical), cerium(III) acetate hydrate (99.9%, $Ce(OAc)_3 \cdot xH_2O$, Sigma-Aldrich), gadolinium(III) acetate hydrate (99.9%, $Gd(OAc)_3 \cdot xH_2O$, Sigma-Aldrich), erbium(III) acetate tetrahydrate (99%, $Er(OAc)_3 \cdot 4H_2O$, Alfa Aesar), and lutetium(III) acetate hydrate (99.9%, $Lu(OAc)_3 \cdot xH_2O$, Alfa Aesar) were used as received.

Synthesis and Purification of RE^{3+}:$CsPbCl_3$ Nanocrystals. RE^{3+}-doped $CsPbCl_3$ NCs ($RE^{3+} = Y^{3+}$, La^{3+}, Ce^{3+}, Gd^{3+}, Lu^{3+}) were synthesized according to the protocol published earlier.[13] In a representative procedure, using Schlenk line techniques, an oven-dried, three-neck flask containing 5 mL of ODE, 0.25 mL of OAm, 1 mL of OA, 75 mg of $Pb(OAc)_2 \cdot 3H_2O$, 12 mg of $Gd(OAc)_3 \cdot xH_2O$, and 280 μL of 1 M CsOAc in EtOH was heated under vacuum at 110 °C for an hour before being flushed with N_2 and heated to 240 °C. Immediately upon reaching 240 °C, a room-temperature TMS–Cl solution (0.5 mL of ODE + 0.2 mL of TMS–Cl) was injected, and the flask was cooled to room temperature using a water bath. The mother liquor was centrifuged at 1318*g* for 5 min, and the supernatant was discarded. The pellet was resuspended in *n*-hexane, and the NCs were flocculated out of the solution with EtOAc. The suspension was centrifuged again for 5 min, and the supernatant was once again discarded. The pellet was resuspended in *n*-hexane and centrifuged for 10 min. The resulting supernatant containing the NCs was stored ambiently in the dark in a glass vial. These NCs stay in solution for ~2 weeks when stored in a dark drawer in an ambient atmosphere, but they can remain stable for several months if stored in an inert atmosphere and dry solvent. For undoped NCs, no $RE(OAc)_3 \cdot xH_2O$ reagent was added to the reaction vessel and only 200 μL of the 1 M Cs^+ solution was used.

Anion Exchange. RE^{3+}:$CsPbBr_3$ NCs were prepared by anion exchange using the chloride NCs described in the previous section according to protocols outlined previously.[19,29,30] In brief, the NCs were dispersed in a dry solvent in a nitrogen-filled glovebox and titrated with 1 M TMS–Br until the desired band gap was obtained, as determined by absorption and PL spectroscopies. The solvent and residual TMS–X were then removed by vacuum evaporation. The NCs were resuspended in dry hexane and stored in the glovebox.

Single-Source Vapor Deposition of 9.3% Gd^{3+}:$CsPbBr_3$ and $CsPbBr_3$ Thin Films. *Materials.* Cesium bromide (99.9%, CsBr, Alfa Aesar), lead(II) bromide (99.9%, $PbBr_2$, Alfa Aesar), and gadolinium(III) bromide (99.9%, $GdBr_3$, Alfa Aesar). *Deposition.* Vapor-deposited thin films were made via rapid thermal evaporation (single-source vapor deposition; SSVD) similar to a process we have reported earlier.[16,31] First, CsBr, $PbBr_2$, and $GdBr_3$ were added in stoichiometric amounts to an agate mortar and pestle and ground for 10 min until a yellow powder was formed. The powder was then annealed in air at 150 °C until it turned orange in color. SSVD was performed in a home-built evaporator comprising a bell jar, a roughing pump, a diffusion pump, and a high-current power supply. Approximately 60 mg of the powder was loaded onto a Ta evaporation boat. The substrates (quartz for VTPL) were sonicated in sodium thiosulfate, water, and hexanes in that order for cleaning. The substrates were suspended 13.5 cm above the evaporation boat. The chamber was evacuated to $\sim 10^{-5}$ torr, and the powder was sublimated by passing a high current through the evaporation boat. The powder was deposited onto the substrate at a rate of ~1000 Å/s over an approximately 2 s window. The samples were immediately transferred to a nitrogen-filled glovebox, where they were annealed at 150 °C for 10 min and subsequently stored until use.

Analytical Characterization. The powder X-ray diffraction data were measured using a Bruker D8 Discover with a high-efficiency IμS microfocus X-ray source for Cu Kα radiation operating at 50,000 mW (50 kV, 1 mA). The samples were prepared by drop-casting NC stock solutions on silicon substrates or by thermally evaporating thin films onto glass substrates. Elemental analysis to determine NC doping concentrations was measured via inductively coupled plasma (ICP) atomic emission spectroscopy using a PerkinElmer 8300. The samples were prepared by digesting the NC powders in concentrated nitric acid with sonication and diluting them in ultrapure H_2O. The TEM images were acquired using an FEI TECNAI F20 microscope operating at 200 kV. A narrow C2 aperture was used to minimize the in situ reduction of Pb^{2+} to Pb^0 by the electron beam. NC stock solutions were diluted by about one-half, and 5 μL of the solution was deposited onto ultrathin carbon-coated copper grids from TED Pella, Inc.

Spectroscopic Measurements. All optical measurements were performed on NCs or thermally evaporated thin films deposited on quartz substrates. The absorption spectra were collected using an Agilent Cary 5000. PL measurements were performed with the sample loaded in a custom-built cryostat cooled by a closed-cycle helium compressor. An LN_2-cooled silicon charge-coupled device was used for PL detection. All spectra were corrected for the wavelength dependence of the instrument response. The chloride samples were excited using a focused 375 nm LED. The bromide samples were excited using a collimated 405 nm LED. Both LEDs were operated as continuous-wave (CW) excitation sources. The VTPL spectra were acquired at temperatures between 14 and 296 K with the sample under continuous illumination. The temperature was allowed to stabilize at each point before data collection. Low-temperature absorption spectra were collected using a Cary 5000 with the NCs drop-cast on a quartz substrate and mounted in the same cryostat used for VTPL measurements.

Time-Resolved PL. For TRPL measurements, the NCs were drop-cast onto quartz substrates and loaded into a closed-cycle helium cryostat. The samples were excited using the third harmonic of a Nd^{3+}:YAG laser (355 nm) firing with a repetition rate of 50 Hz and having a 30 ps pulse width. The excitation flux was kept constant at 60 nJ/pulse. A Hamamatsu streak camera was used for PL detection. Temporal windows of 20 ns, 500 ns, 5 μs, and 50 μs were measured.

https://doi.org/10.1021/acs.chemmater.2c00132
Chem. Mater. XXXX, XXX, XXX−XXX

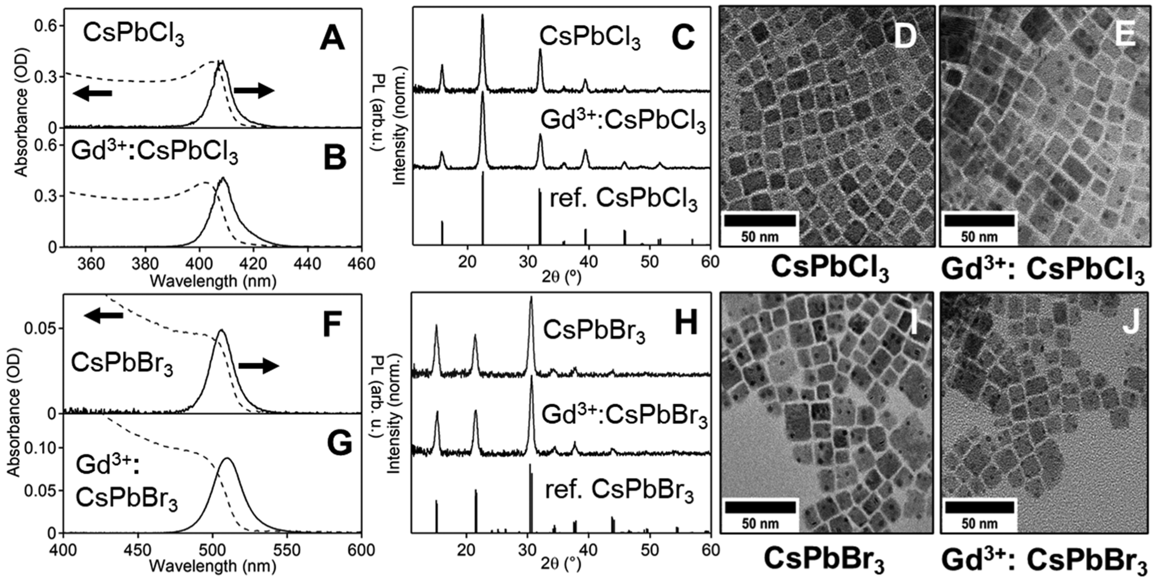

Figure 1. Physical characterization of $CsPbX_3$ and Gd^{3+}:$CsPbX_3$ NCs. (A,B) Room-temperature absorption and PL spectra of $CsPbCl_3$ (A) and 7.7% Gd^{3+}:$CsPbCl_3$ (B) NCs. (C) X-ray diffraction patterns of the NCs from (A,B). Reference orthorhombic $CsPbCl_3$.[34] (D,E) TEM images of the NCs from (A, B). Scale bar: 50 nm. (F,G) Room-temperature absorption and PL spectra of $CsPbBr_3$ (F) and 7.7% Gd^{3+}:$CsPbBr_3$ (G) NCs. (H) X-ray diffraction patterns of the NCs from (F,G). Reference orthorhombic $CsPbBr_3$.[34] (I,J) TEM images of the NCs from (F,G). Scale bar: 50 nm.

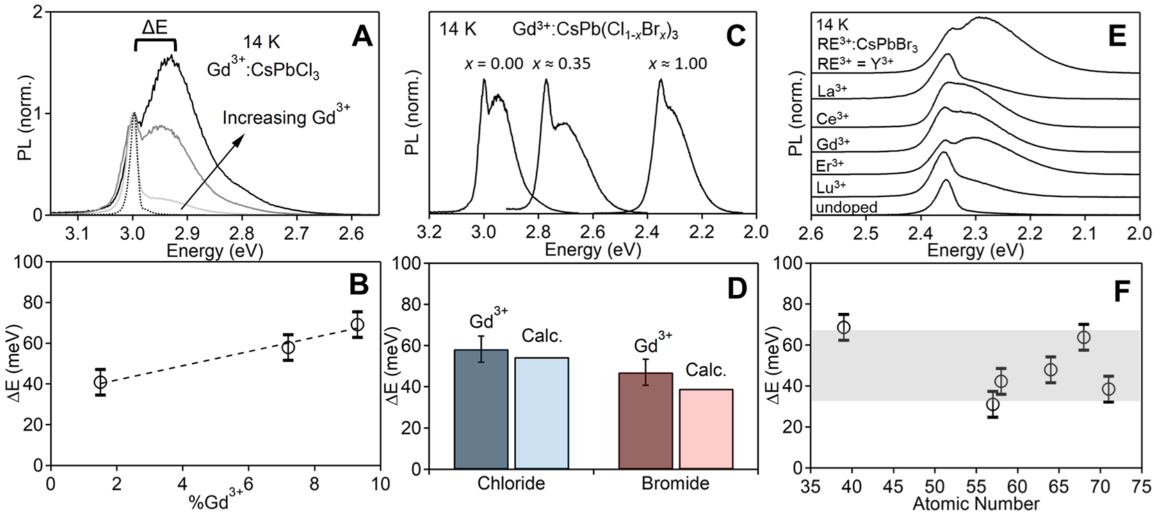

Figure 2. Low-temperature PL of RE^{3+}:$CsPb(Cl_{1-x}Br_x)_3$ NCs. (A) 14 K PL spectra of a series of Gd^{3+}:$CsPbCl_3$ NCs with different Gd^{3+} doping levels (1.5, 7.2, and 9.3%), collected using a CW 375 nm excitation. (B) Exciton-to-NBE PL splitting energy, ΔE, plotted vs the Gd^{3+} B-site cation mole fraction, from (A). The dashed line shows a linear best fit of the data, yielding the relationship $\Delta E = [35.0 + 3.5 \times (\%\ Gd^{3+})]$ meV. (C) 14 K PL spectra of 7.1% Gd^{3+}:$CsPb(Cl_{1-x}Br_x)_3$ (x = 0.00, 0.35, 1.00) NCs, collected using 375 nm (x = 0) or 405 nm ($x \approx$ 0.35, 1.00) excitation. (D) Comparison of the experimental ΔE values for Gd^{3+}-doped $CsPbCl_3$ and $CsPbBr_3$ NCs from (C) with calculated binding energies of the exciton to V_{Pb} in $CsPbCl_3$ and $CsPbBr_3$ (see text). (E) 14 K PL spectra of $CsPbBr_3$ NCs doped with 10.5% Y^{3+}, 8.5% La^{3+}, 7.6% Ce^{3+}, 10.3% Gd^{3+}, 9.6% Er^{3+}, and 7.4% Lu^{3+}. The bottom spectrum is of undoped $CsPbBr_3$ NCs. (F) ΔE plotted vs the RE^{3+} atomic number for the series of RE^{3+}-doped $CsPbBr_3$ NCs from (E). The gray bar is a guide to the eye. The error bars on the experimental ΔE values are estimated from the fitting analysis (Figures S2 and S3).

■ RESULTS AND DISCUSSION

Nanocrystals. Figure 1A,B shows the room-temperature absorption and PL data for $CsPbCl_3$ and 7.7% Gd^{3+}:$CsPbCl_3$ NCs, respectively. The doping concentrations are determined analytically using ICP−optical emission spectroscopy and reported with respect to all B-site cations. Despite the large Gd^{3+} content in the doped NCs, their absorption spectrum closely resembles that of undoped $CsPbCl_3$ NCs. The room-temperature PL spectrum of the Gd^{3+}-doped NCs also closely matches that of the undoped $CsPbCl_3$ NCs. The Stokes shift between the excitonic absorption and PL maxima is small (∼22 meV peak-to-peak) for both samples. Figure 1C plots the X-ray diffraction data collected for the NCs from Figure 1A,B. The observation of very similar diffraction angles despite high Gd^{3+} incorporation is attributed to the offsetting structural effects of charge-compensating Pb^{2+} vacancies.[32] Figure 1D,E shows representative TEM images of the NCs from Figure 1A,B, respectively. The $CsPbCl_3$ and 7.7% Gd^{3+}:$CsPbCl_3$ NCs have an average edge-to-edge length of 10.9 ± 2.1 and 11.5 ± 4.0 nm, respectively. These NCs are larger than the $CsPbCl_3$ Bohr

https://doi.org/10.1021/acs.chemmater.2c00132
Chem. Mater. XXXX, XXX, XXX−XXX

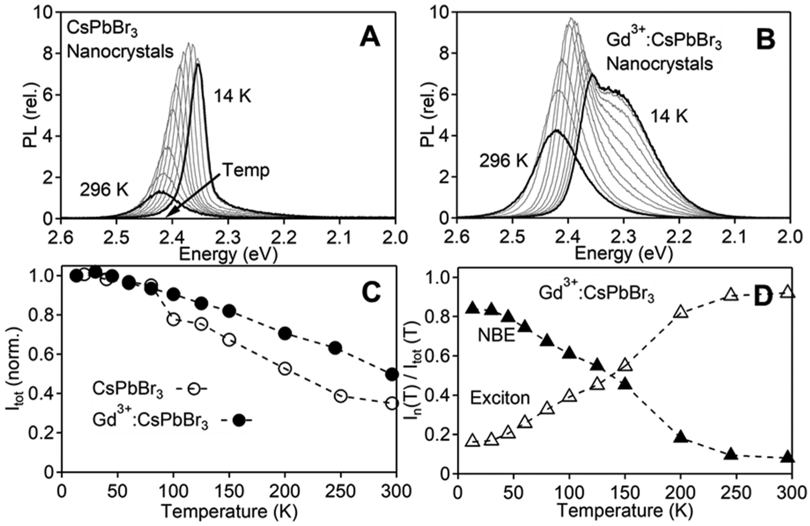

Figure 3. VTPL of $CsPbBr_3$ and Gd^{3+}:$CsPbBr_3$ NCs. PL spectra measured from 14 to 296 K of (A) $CsPbBr_3$ and (B) 7.7% Gd^{3+}:$CsPbBr_3$ NCs, collected using a CW 405 nm (3.06 eV) excitation. (C) Total integrated PL intensity plotted as a function of temperature, normalized to the PL intensity at 14 K (open circles: $CsPbBr_3$ NCs; solid circles: 7.7% Gd^{3+}:$CsPbBr_3$ NCs). The dashed lines are guides to the eye. (D) Temperature dependence of the integrated exciton (open triangles) and NBE (solid triangles) PL intensities from the 7.7% Gd^{3+}:$CsPbBr_3$ NC data in (B), normalized to the total PL intensity at each temperature.

exciton diameter of ~5 nm,[33] and consequently, no quantum confinement is expected. Overall, Gd^{3+}-doped and undoped $CsPbCl_3$ NCs are thus essentially indistinguishable in these measurements.

The same similarity is found between doped and undoped $CsPbBr_3$ NCs. Figure 1F,G shows the room-temperature absorption and PL spectra of $CsPbBr_3$ and 7.7% Gd^{3+}:$CsPbBr_3$ NCs made from the parent chloride NCs by anion exchange. The room-temperature absorption and PL spectra of the Gd^{3+}-doped NCs again closely resemble those of the undoped $CsPbBr_3$ NCs. Likewise, Figure 1H shows X-ray diffraction data collected for the NCs from Figure 1F,G, and these also look indistinguishable. Figure 1I,J shows representative TEM images of the NCs from Figure 1F,G. The $CsPbBr_3$ and 7.7% Gd^{3+}:$CsPbBr_3$ NCs have average edge-to-edge lengths of 11.6 ± 2.4 and 12.9 ± 3.8 nm, respectively. These sizes relative to those in Figure 1D,E are consistent with expectations from the replacement of chloride anions with larger bromide anions during anion exchange. The $CsPbBr_3$ NCs are larger than the $CsPbBr_3$ Bohr exciton diameter of ~7 nm,[33] and hence, quantum confinement effects are again not expected.

Although the PL spectra of Gd^{3+}-doped and undoped $CsPb(Cl_{1-x}Br_x)_3$ NCs look essentially identical at room temperature, major differences emerge at low temperatures. Figure 2A plots 14 K PL spectra of a series of Gd^{3+}:$CsPbCl_3$ NCs with doping concentrations ranging from 0.0 to 9.3%. A small low-energy tail is observed in the 14 K PL spectrum of the undoped $CsPbCl_3$ NCs that is attributable to radiative surface trap states (Figure S1). As doping increases, there is a dramatic increase in the PL intensity of a near-band-edge (NBE) feature ~50 meV below the excitonic PL. The NBE-to-exciton PL intensity ratio (I_{NBE}/I_{exc}) increases 20-fold from 1.5 to 9.3% Gd^{3+}, demonstrating that this NBE emission is indeed induced by Gd^{3+} doping. Figure 2B summarizes the exciton-to-NBE splitting energies (ΔE) from the data in Figure 2A, plotting ΔE versus the Gd^{3+} doping concentration. As observed in this plot, ΔE increases slightly with increasing doping concentration, growing by ~3.5 meV per %Gd^{3+}. Overall, the NBE emission is qualitatively unchanged between 1.5 and 9.3% Gd^{3+}. Importantly, the half-filled ($4f^7$) ground electronic configuration of Gd^{3+} pushes its lowest-energy *f–f* and charge-transfer transitions all to very high energies (~4 eV), well above the perovskite energy gaps investigated here, so we can conclude that this NBE emission does not come from any electronic excited state of Gd^{3+} itself.

To explore this NBE emission further, we examined its dependence on the $CsPb(Cl_{1-x}Br_x)_3$ energy gap, using anion exchange to tune that gap. ICP measurements performed before and after anion exchange and washing show no statistically significant change in the dopant concentration. Figure 2C plots the 14 K PL spectra of ~7.1% Gd^{3+}:$CsPb(Cl_{1-x}Br_x)_3$ NCs at three different bromide concentrations (x = 0.00, ~0.35, 1.00), all stemming from the same parent 7.1% Gd^{3+}:$CsPbCl_3$ NCs (x = 0.00). The NBE PL remains distinct below the excitonic PL in all compositions. When comparing x = 0.00 to x = 1.00, the NBE feature appears to be closer to the exciton in the latter. The NBE band shape is also noticeably broader in the intermediate (x = 0.35) spectrum, suggesting that its energy is sensitive to the microscopic heterogeneities introduced in the mixed-halide composition. Figure 2D illustrates that ΔE versus x decreases from 58 meV at x = 0.00 to 47 meV at x = 1.00.

To test the assertion that the NBE PL observed in Gd^{3+}-doped $CsPb(Cl_{1-x}Br_x)_3$ NCs does not come from any electronic excited state of Gd^{3+} itself, we compare the low-temperature PL spectra of a series of RE^{3+}-doped $CsPbBr_3$ NCs, where RE^{3+} = Y^{3+}, La^{3+}, Ce^{3+}, Gd^{3+}, Lu^{3+}. Most of these RE^{3+} ions possess either closed- or half-filled *f*-shell configurations. Ce^{3+} ($4f^1$) often shows an *f–d* transition at relatively low energies, but this transition falls outside of the $CsPbBr_3$ band gap.[35] Figure 2E plots the 14 K PL spectra of this series of samples in comparison with the spectrum of undoped $CsPbBr_3$ NCs. Although there are differences in I_{NBE}/I_{exc}, the characteristic NBE PL is observed in *every* RE^{3+}-doped NC sample of this series. Moreover, this NBE PL is not limited to spectroscopically innocent RE^{3+} dopants: Figure 2E also plots the low-temperature PL spectrum of 9.6% Er^{3+}:$CsPbBr_3$ NCs, and this, too, shows very similar NBE PL. The

https://doi.org/10.1021/acs.chemmater.2c00132
Chem. Mater. XXXX, XXX, XXX−XXX

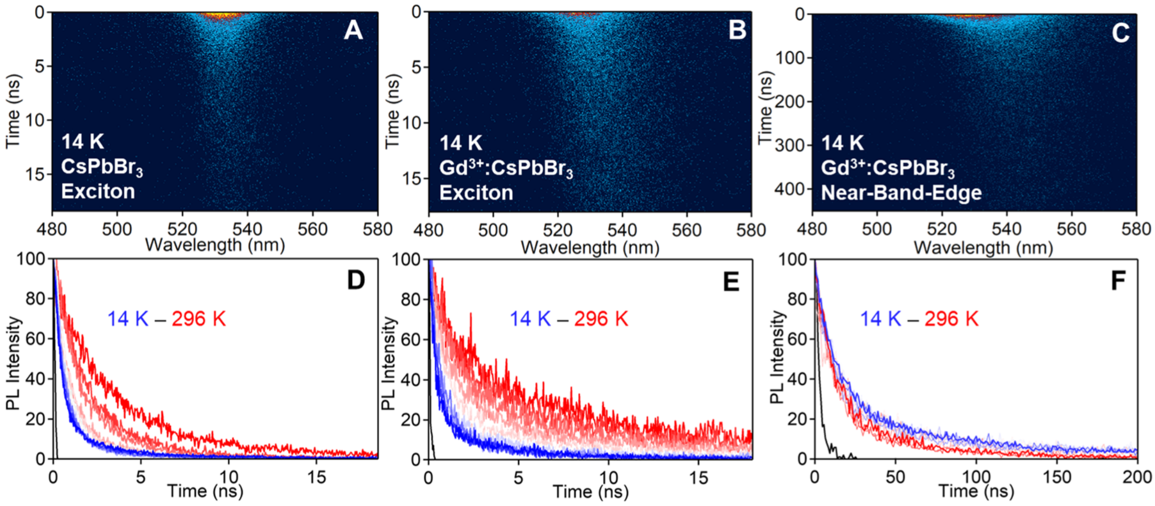

Figure 4. VT TRPL of $CsPbBr_3$ and Gd^{3+}:$CsPbBr_3$ NCs. Streak-camera images of the 14 K TRPL from (A) $CsPbBr_3$ NCs and (B,C) 7.7% Gd^{3+}:$CsPbBr_3$ NCs. Note the long timescale of (C). Similar streak-camera data were collected at multiple temperatures between 14 K and room temperature. (D) VT exciton PL decay traces for the $CsPbBr_3$ NCs from (A), measured from 14 K (blue) to room temperature (red), extracted from streak-camera data. (E) VT exciton PL decay traces for the 7.7% Gd^{3+}:$CsPbBr_3$ NCs, as in (D). (F) VT NBE PL decay traces for the 7.7% Gd^{3+}:$CsPbBr_3$ NCs, as in (C). Note the long timescale of (C). The black curves in (D−F) show the instrument response functions for each measurement. For the Gd^{3+}:$CsPbBr_3$ NC decay traces in (E,F), the exciton PL decay was integrated between 510−525 nm (13−80 K), 500−520 nm (100−150 K), or 490−515 nm (200−296 K), and the NBE PL was integrated between 535−585 nm (13−30 K), 530−575 nm (45−150 K), or 520−555 nm (200−296 K).

dependence of the NBE PL on the halides in the Er^{3+}:$CsPb(Cl_{1-x}Br_x)_3$ NCs is essentially identical to that shown in Figure 2C (Figure S4). No other lower-energy *f*–*f* emission is observed in any of these Er^{3+}-doped NCs, consistent with previous reports.[24,28] Figure 2F plots ΔE versus RE^{3+} atomic number for this RE^{3+}:$CsPbBr_3$ NC series, showing that in all cases, $\Delta E = 49 \pm 15$ meV. This result allows the conclusion that this NBE defect state is ubiquitous in RE^{3+}-doped $CsPbX_3$ perovskite NCs. We thus equate the spectroscopic energy difference (ΔE) with the binding energy (E_b) of an exciton to a dopant-induced defect.

To understand the properties of this NBE state in greater detail, we performed VTPL measurements. Figure 3A plots the VTPL spectra of the $CsPbBr_3$ NCs collected from 14 to 296 K. Like in the undoped $CsPbCl_3$ NCs, the low-temperature spectrum shows a weak tail below the exciton, attributed to surface states (Figure S1). Figure 3B plots VTPL spectra collected over the same temperature range for 7.7% Gd^{3+}:$CsPbBr_3$ NCs. In both samples, I_{exc} increases with increasing temperature until ~90 K before turning over and decreasing again up to room temperature. In contrast, I_{NBE} in the Gd^{3+}:$CsPbBr_3$ NCs only decreases as the temperature increases, and by ~200 K, this feature is no longer discernible. Figure 3C plots the total integrated PL intensity (I_{tot}) for both samples as a function of temperature and normalized to the intensity at 14 K. Despite the large spectral changes observed in the doped NC spectra, both samples show essentially the same gradual decrease of I_{tot} with increasing temperature. Figure 3D plots I_{exc}/I_{tot} and I_{NBE}/I_{tot} separately at each temperature for the Gd^{3+}:$CsPbBr_3$ NCs. I_{NBE}/I_{tot} is highest at 14 K and decreases as the temperature is raised. I_{exc}/I_{tot} shows opposite temperature dependence, such that at room temperature, the PL spectrum is essentially entirely excitonic. Remarkably similar results were also found in a VTPL comparison of $CsPbCl_3$ and Gd^{3+}:$CsPbCl_3$ NCs (Figure S5). These data show that the overall temperature dependence is independent of Gd^{3+} doping and must therefore relate to other thermally activated nonradiative recombination pathways native to $CsPb(Cl_{1-x}Br_x)_3$ NCs, but changing the temperature dramatically alters the relative probabilities of NBE versus excitonic PL. Because of its lower energy, the NBE PL intensity increases as the temperature is lowered. These data also suggest that these two states are not in simple thermal equilibrium with one another, however, because in this limit, no excitonic PL would be observed at 14 K, given the ~50 meV binding energy of the NBE state (Figure S11).

To examine the dynamics associated with this NBE state, TRPL measurements were performed at various temperatures and the results are summarized in Figure 4. Figure 4A,B plots representative streak-camera images of the first 20 ns of PL decay from $CsPbBr_3$ and 7.7% Gd^{3+}:$CsPbBr_3$ NCs, respectively, collected at 14 K. Figure 4C plots a streak-camera image of the same Gd^{3+}:$CsPbBr_3$ NC PL decay but now covering a much longer time window (>400 ns). Over the first 20 ns, the two samples show similar excitonic PL decay. Whereas no substantial further PL is observed in the undoped NCs, the Gd^{3+}:$CsPbBr_3$ NCs show additional NBE PL decay at lower energy and over longer times. Figure 4D,E plots excitonic PL decay traces for the undoped $CsPbBr_3$ and 7.7% Gd^{3+}:$CsPbBr_3$ NCs taken from such streak-camera images and now includes data collected at several temperatures from 14 to 296 K. The doped and undoped NCs show very similar temperature dependence of their excitonic PL decay. At low temperatures, ~90% of the excitonic PL is depleted within ~2.5 ns for both samples. In both samples, the excitonic PL decay gets progressively slower as the temperature is raised such that, at room temperature, it takes nearly 8 ns to deplete 90% of the excitonic PL in the undoped NCs and nearly 18 ns in the Gd^{3+}-doped NCs. Figure 4F plots the PL decay curves for the NBE PL of the 7.7% Gd^{3+}:$CsPbBr_3$ NCs measured at the same series of temperatures. The NBE PL decay is much slower than the excitonic PL decay, and it appears to be independent of temperature until ~150 K, above which it begins to shorten slightly (see the Supporting Information for complete

https://doi.org/10.1021/acs.chemmater.2c00132
Chem. Mater. XXXX, XXX, XXX−XXX

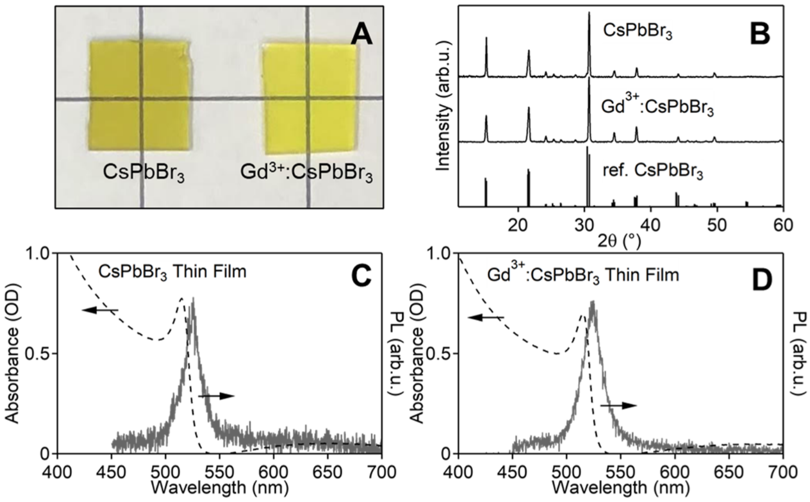

Figure 5. Characterization of thermally evaporated $CsPbBr_3$ and Gd^{3+}:$CsPbBr_3$ thin films. (A) Photo of representative thermally evaporated perovskite thin films deposited on glass substrates. Left: $CsPbBr_3$; Right: 9.3% Gd^{3+}:$CsPbBr_3$. Grid spacing: 2 cm. Both films are ∼0.2 μm thick. (B) X-ray diffraction data for $CsPbBr_3$ and 9.3% Gd^{3+}:$CsPbBr_3$ thin films. A reference X-ray diffraction pattern for orthorhombic $CsPbBr_3$ is included for comparison.[34] Room-temperature absorption and PL spectra of representative (C) undoped $CsPbBr_3$ and (D) 9.3% Gd^{3+}-doped $CsPbBr_3$ thin films.

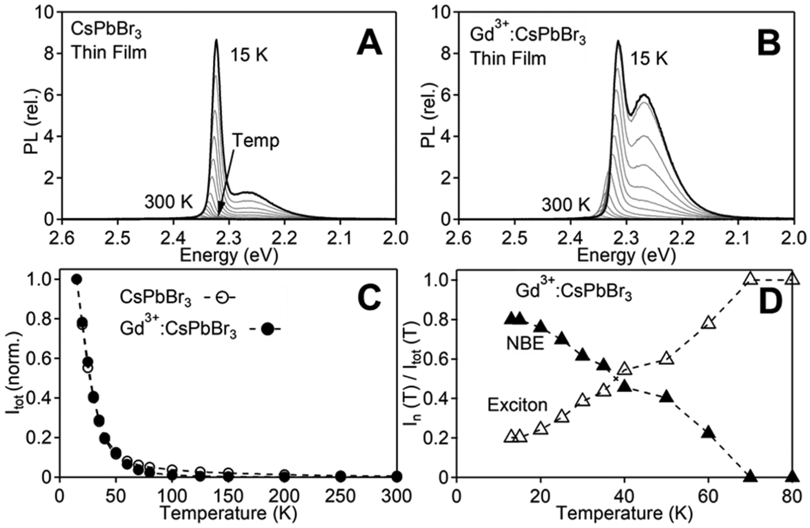

Figure 6. VTPL of thermally evaporated $CsPbBr_3$ and Gd^{3+}:$CsPbBr_3$ thin films. PL spectra of the (A) 9.3% Gd^{3+}-doped $CsPbBr_3$ thin film and (B) $CsPbBr_3$ thin film collected at the temperatures of 15, 20, 25, 30, 35, 40, 45, 50, 60, 70, 80, 100, 125, 150, 200, 250, and 300 K. (C) Integrated PL intensities from (A,B), plotted vs temperature. Open circles: $CsPbBr_3$; filled circles: 9.3% Gd^{3+}:$CsPbBr_3$. (D) Temperature dependence of the integrated exciton (open triangles) and NBE (solid triangles) PL intensities from the Gd^{3+}:$CsPbBr_3$ data in (B), normalized to the total PL intensity at each temperature.

analysis). Power-law behavior is noted for the last ∼10% of NBE emission (Figure S6), suggesting delayed PL. Notably, the exciton and NBE decay dynamics never converge, as would be required in the limit of thermal equilibrium. These TRPL data thus confirm the conclusion drawn from the VTPL spectra that the exciton and NBE populations are not in simple thermal equilibrium with one another; a subset of excitons appears to be unaffected by the introduction of Gd^{3+}.

Thin Films. To test the potential role of high surface-to-volume ratios in generating this NBE PL, we prepared and examined the spectroscopy of analogous thermally evaporated thin films of $CsPbBr_3$ and Gd^{3+}:$CsPbBr_3$. Figure 5A shows a photograph of representative thin films of $CsPbBr_3$ and 9.3% Gd^{3+}:$CsPbBr_3$, placed on top of a white paper with drawn lines to illustrate their color, size, and transparency. Both perovskite films are ∼0.2 μm thick. The films possess excellent optical quality, showing minimal scattering. Figure 5B plots X-ray diffraction data collected for the samples in Figure 5A. Both samples show diffraction consistent with orthorhombic $CsPbBr_3$. Figure 5C,D plots room-temperature absorption and PL spectra of the undoped and doped thin films, respectively. Both absorption spectra show a well-defined exciton peak at ∼515 nm, and both also show sub-band-gap interference fringes consistent with the film thickness. Weak exciton emission is observed from both samples at room temperature. Overall, the two samples appear to be very similar at room temperature, just as the doped and undoped NCs did.

Figure 6A,B plots VTPL spectra of the $CsPbBr_3$ and 9.3% Gd^{3+}:$CsPbBr_3$ thin films measured from 15 to 296 K. Both samples show a distinct NBE emission feature ΔE ∼ 50 meV

https://doi.org/10.1021/acs.chemmater.2c00132
Chem. Mater. XXXX, XXX, XXX−XXX

Table 1. Parameterized Ab Initio Constants and Exciton Energies in $CsPbX_3$ (X = Cl, Br, I) Doped with RE^{3+} Impurities[a]

	E_{LO} [meV]	ϵ_s	ϵ_∞	m_h^*	m_e^*	E_{AX} [meV]	E_X [meV]	E_X^{exp} [meV]	ΔE^{calc} [meV]	ΔE^{exp} [meV]
$CsPbCl_3$	26	17.5	3.7	0.28	0.30	−158.9	−104.4	−72,[43] −64[45]	54.5	58 ± 6
$CsPbBr_3$	18	18.6	4.5	0.20	0.21	−79.3	−40.3	−38,[43] −33[44]	39.0	47 ± 6
$CsPbI_3$	14	22.5	5.5	0.20	0.18	−44.9	−21.3	−15[44]	23.6	N/A

[a]Experimental defect-binding energies (ΔE^{exp}, Gd^{3+}) from Figure 2 are compared with the difference between free-exciton and V_{Pb}^{2-}-bound-exciton energies, $\Delta E^{calc} = |E_{AX} - E_X|$.

below the exciton emission, but this feature is 4 times larger in the Gd^{3+}-doped sample at 15 K. The NBE PL band shape is narrower in the Gd^{3+}-doped thin film than in the corresponding NCs, consistent with the conclusion drawn above that this feature is susceptible to inhomogeneous broadening. These results demonstrate that this NBE PL is indeed induced by Gd^{3+} doping. Because the surface-to-volume ratios of these thin films are orders of magnitude smaller than in the NCs, we conclude that the NBE PL is not associated with surfaces. These results also suggest that the NBE PL induced by Gd^{3+} doping has a native analogue in undoped bulk $CsPbX_3$, that is, the native defect responsible for the NBE PL observed in the undoped $CsPbBr_3$ data of Figure 6A. A similar sub-band-gap PL feature has indeed been observed in other bulk $CsPbBr_3$ samples, but its assignment varies. It has been attributed to bound excitons at structural defects and to a Rashba effect induced by dynamic fluctuations in the position of the A-site cation, Cs^+.[36−38] For both samples in Figure 6, I_{exc} decreases rapidly with increasing temperature, in contrast to the NCs. Figure 6C plots $I_{tot}(T)/I_{tot}(15\text{ K})$ as a function of temperature for each sample. Both data sets show the same rapid decrease in I_{tot} between 15 and 80 K, indicative of efficient thermally activated nonradiative recombination. At room temperature, both samples have lost over 99% of their 15 K PL intensity. Figure 6D plots I_{exc}/I_{tot} and I_{NBE}/I_{tot} for the Gd^{3+}:$CsPbBr_3$ thin film, measured from 15 K to room temperature. I_{NBE}/I_{tot} is highest at 15 K and decreases as the temperature is raised. By 40 K, I_{exc} exceeds I_{NBE}, and the latter drops to nearly 0 by ~70 K. The values of ΔE and the temperature dependence of both I_{exc}/I_{tot} and I_{NBE}/I_{tot} are thus very similar to those observed in the analogous NCs, despite the fact that the thin-film emission is far more susceptible to thermal quenching. This observation supports the attribution of this NBE PL feature to the same RE^{3+}-induced defect in both NC and thin-film samples.

Calculated Exciton-Binding Energies. Previously,[32] we applied first-principles electronic-structure calculations and a thermodynamic model to investigate the effects of Yb^{3+} doping in single-crystalline $CsPbCl_3$. These calculations identified conditions under which locally bound charge-neutral $[2Yb_{Pb} + V_{Pb}]^0$ defect complexes become prevalent and also revealed significant $[Yb_{Pb} + V_{Pb}]^-$ defect formation. Examination of the electronic properties of such defect complexes showed shallow binding of both electrons and holes. The predicted defect structures arise from the electrostatics of aliovalent doping and were thus largely independent of the specific RE^{3+} dopant, in good agreement with the experiment (Figure 2). We now show that the shallow exciton binding predicted by these calculations follows the same trend, as observed experimentally in Figure 2C,D.

To assist in interpretation of the experimental data, we consider here charge-carrier trapping to a shallow defect. For illustration, we assume that a doubly charged Pb^{2+} vacancy (V_{Pb}^{2-}) provides the dominant contribution to an exciton bound by the charge-neutral $[2RE_{Pb} + V_{Pb}]^0$ defect complex, although the same conclusions are drawn for any shallow defect. In the Born−Oppenheimer adiabatic approximation, this shallow acceptor-bound exciton (AX) is described by the effective Hamiltonian

$$H_{AX} = -\frac{1}{2}\nabla_1^2 - \frac{1}{2\sigma}\nabla_2^2 - \frac{q_d}{r_1} + \frac{q_d}{r_2} + V_H(r_{12}) \tag{1}$$

written in atomic units with respect to the electron effective mass (m_e^*) and the static dielectric constant (ϵ_s). The distances separating the conduction-band (CB) electron and valence-band (VB) hole from the V_{Pb}^{2-} are denoted r_1 and r_2, respectively, and the ratio of their effective masses is $\sigma = m_h^*/m_e^*$. The nominal charge state of V_{Pb}^{2-} is $q_d = -2$, and its interactions with the excited electron−hole pair are screened according to ϵ_s of the material. In lead-halide perovskites, large differences between static and high-frequency (ϵ_∞) dielectric constants imply strong Fröhlich couplings

$$\alpha_{e,h} = \frac{e^2}{\hbar}\left(\frac{1}{\epsilon_\infty} - \frac{1}{\epsilon_s}\right)\sqrt{\frac{m_{e,h}^*}{2E_{LO}}} \tag{2}$$

between charge carriers and longitudinal optical (LO) phonons, with characteristic excitation energy, E_{LO}. To account for phonon screening effects, we model the electron−hole interaction following the work of Haken[39,40]

$$V_H(r) = -\frac{e^2}{\epsilon_s r} - \frac{e^2}{2r}\left(\frac{1}{\epsilon_\infty} - \frac{1}{\epsilon_s}\right)(e^{-r/l_h} + e^{-r/l_e}) \tag{3}$$

where effective length scales for electron and hole polarons are defined by

$$l_{e,h} = \sqrt{\hbar^2/2m_{e,h}^* E_{LO}} \tag{4}$$

Dynamical screening by LO phonons also leads to renormalized effective masses[41]

$$\tilde{m}_{e,h}^* = m_{e,h}^*(1 + \alpha_{e,h}/6) \tag{5}$$

which are accounted for in the kinetic energy terms in H_{AX}. For consistency, we treat the free exciton (X) with the same level of theory, described by the Hamiltonian

$$H_X = -\frac{1}{2}\nabla^2 + V_H(r) \tag{6}$$

in the center-of-mass frame of the free exciton. To parameterize these models, we used ab initio dielectric constants, effective masses, and LO phonon energies reported[42] for $CsPbX_3$ (X = Cl, Br, I) in the low-temperature, orthorhombic ($Pnma$) perovskite phase. These quantities were calculated from density functional theory (DFT) and the GW Bethe−Salpeter equation (GW-BSE) method.[42] The ground states of H_{AX} and H_X were determined by the variational method.[32]

https://doi.org/10.1021/acs.chemmater.2c00132
Chem. Mater. XXXX, XXX, XXX−XXX

Table 1 summarizes the results of our variational ground-state calculations of free-exciton (E_X) and V_{Pb}^{2-}-bound-exciton (E_{AX}) energies, along with the specific ab initio parameters used for these calculations. Table 1 also includes the experimental exciton-binding energies (E_X^{exp}) for comparison.[43−45] For $CsPbBr_3$, we find good agreement between our calculated E_X and the experimental values.[43−45] Although the discrepancy is larger for $CsPbCl_3$, it is smaller than that for other reported computational values (e.g., 146 meV in ref 42). We note that the authors of ref 42 found reductions of 12% to 17% in the exciton binding energy in the $CsPbX_3$ series due to phonon screening.

From these calculations, the energy differences $|E_{AX} - E_X|$ are then used to approximate the splitting energy between exciton and NBE emission probed experimentally. The calculations show that $\Delta E^{calc} = |E_{AX} - E_X|$ decreases as the halide atomic number increases in the $CsPbX_3$ series. This trend essentially reflects the changing dielectric constants across this series: Coulombic interactions are more effectively screened in lattices with heavier halides. Phonon screening does contribute to the predicted values of ΔE^{calc}, however. For example, the computed value of ΔE^{calc} in $CsPbCl_3$ neglecting phonon screening is 108.6 meV, compared to 54.5 meV in Table 1.

The calculated splitting energies are compared with the experimental values of ΔE in Table 1 and Figure 2D. The quantitative agreement between the calculated and experimental magnitudes of ΔE may be fortuitous, given that these calculations have assumed that exciton binding is dominated by V_{Pb}^{2-}, whereas $RE_{Pb}{}^{+}$ may also contribute significantly. For example, solving eq 3 for trapping an exciton to a single shallow +1 donor defect such as RE_{Pb} yields $\Delta E^{calc} = |E_{DX} - E_X|$ = 18.1 (Cl), 10.0 (Br), and 7.4 (I) eV, and carrier binding to a more complex defect cluster involving both donor and acceptor defects is even more complicated. Critically, the calculations predict the decrease in ΔE with increasing halide atomic number well, from which we conclude that the decrease in ΔE observed in Figure 2 on changing from RE^{3+}:$CsPbCl_3$ to RE^{3+}:$CsPbBr_3$ results from increased dielectric screening rather than from any specific electronic-structure property of the trap state itself (e.g., relative electron vs hole binding). We note that we were unsuccessful in our attempts to synthesize RE^{3+}:$CsPbI_3$ NCs via anion exchange or direct methods; these calculations thus provide a prediction for ΔE in $CsPbI_3$ that remains to be tested experimentally.

RE^{3+} Doping, Shallow Defects, and Related Observations. The data and analysis presented above describe the appearance of a prominent NBE PL feature in $CsPb(Cl_{1-x}Br_x)_3$ NCs upon doping with RE^{3+} ions. Similar NBE PL features have been reported for other forms of $CsPbX_3$, both doped and undoped (e.g., Figure 6A), but clear consensus about the origins of this NBE PL has not yet emerged. In many cases, this NBE PL has been attributed to surfaces. In $CsPbBr_3$ nanosheets, for example, low-temperature PL reveals a broad feature ~35 meV below the exciton that was attributed to trapped excitons.[46] Nanoscale $CsPbBr_3$ structures formed in Pb^{2+}-doped CsBr single crystals show a similar feature, attributed to trapping at $CsPbBr_3$/CsBr interfaces or electronic transitions associated with Pb^{2+}.[47] $CsPbBr_3$ NCs have also shown a similar NBE PL feature at 80 K (~70 meV below the exciton emission with a 10 ns lifetime), attributed to donor−acceptor pair luminescence involving surface-trapped carriers.[48] Similar NBE PL was also observed in the low-temperature spectra of La^{3+}:$CsPbCl_3$ NCs[13] and single crystals.

The results presented here demonstrate that RE^{3+} doping of $CsPbX_3$ universally generates such an NBE defect state. The RE^{3+} series examined here spans all of the lanthanides and additionally includes the $4d^0$ Y^{3+} ion as a pseudo-lanthanide; yet, essentially the same NBE PL is observed in all cases, independent of the specific RE^{3+} dopant. Most of the RE^{3+} ions examined here possess no internal *f*−*f* or charge-transfer excited states within the perovskite energy gap, indicating that this NBE PL must arise from a perturbation of the $CsPbX_3$ lattice and not from the dopant itself. The observation of the same NBE PL in Er^{3+}-doped $CsPb(Cl_{1-x}Br_x)_3$ NCs extends this conclusion to include RE^{3+} ions that do possess midgap internal states. We conclude that the formation of this NBE defect state is a universal consequence of such aliovalent doping in perovskite $CsPbX_3$.

One common challenge in studying defects experimentally is their irreproducibility. The NBE defect generated by RE^{3+} doping is robust in ways not observed for the analogous native defects. For example, the native NBE PL in undoped $CsPbBr_3$ NCs can be changed and even completely suppressed through surface modification, whereas the NBE PL of RE^{3+}-doped NCs is insensitive to the same surface chemistry (Figure S1). This result suggests that the NBE state in RE^{3+}-doped $CsPbX_3$ resides within the internal volume of the lattice, a conclusion supported by the observation that similar NBE PL is induced by RE^{3+} doping in thin films with vastly smaller surface-to-volume ratios. These observations indicate that doping with spectroscopically innocent RE^{3+} ions offers a powerful tool for generating well-behaved defects in lead-halide perovskites.

The microscopic structure of this defect remains unclear. Recent first-principles electronic-structure calculations probing defect formation in Yb^{3+}-doped $CsPbCl_3$ have identified several locally bound and dissociated configurations of $[2Yb_{Pb} + V_{Pb}]^0$ with similar thermodynamics and have predicted the prevalence of a series of closely related charge-neutral $[Yb-V_{Pb}-Yb]^0$ defect clusters at high Yb^{3+} concentrations.[32] DFT calculations on such clusters suggest their role as shallow electron traps rather than shallow hole traps.[49] DFT has also been used to predict that substitution of Pb^{2+} with Ce^{3+} in $CsPbBr_3$ (in the absence of additional charge-compensating defects) does not induce deep traps that quench exciton PL but rather promotes emission at or near the band edge.[6] An intriguing alternative possibility is that RE^{3+} dopants and their associated defects may locally polarize the perovskite lattice, lowering the site symmetry and thereby enhancing the Rashba effect (a spin band splitting in k-space occurring in materials with large spin orbit coupling and lacking inversion symmetry[50]). In $CsPbBr_3$ nanocrystals, however, typical Rashba splittings observed in magneto-optical measurements are only ~1−2 meV,[51] that is, much smaller than the binding energies observed here. Preliminary magneto-PL measurements on these RE^{3+}-doped $CsPb(Cl_{1-x}Br_x)_3$ samples do show circular polarization of the NBE emission (Figure S11), but further measurements will be required to determine whether this polarization could be associated with a Rashba effect or just reflects the natural spin characteristics of a defect-bound exciton in this lattice.

These results may also have significant implications for understanding the mechanism of quantum cutting in Yb^{3+}:$CsPb(Cl_{1-x}Br_x)_3$ NCs and thin films. In this process, perovskite photoexcitation leads to energy-transfer excitation

https://doi.org/10.1021/acs.chemmater.2c00132
Chem. Mater. XXXX, XXX, XXX−XXX

of two Yb^{3+} dopants simultaneously, allowing the PL quantum yields to exceed 100%. Spectroscopic studies have identified signatures of an intermediate state in this energy-transfer process, residing between the $CsPb(Cl_{1-x}Br_x)_3$ exciton and the Yb^{3+} *f*–*f* excited states.[13,23] This intermediate state depletes the exciton population on the picosecond timescale and passes that energy to Yb^{3+} with a time constant of ~8 ns at room temperature.[13,23] The observations detailed above indicate that an NBE defect state is formed upon Yb^{3+} doping, even though NBE PL has not been observed in Yb^{3+}:$CsPb(Cl_{1-x}Br_x)_3$, presumably because of rapid energy capture by Yb^{3+}. The ubiquitous NBE state described here appears to be consistent with all of the known properties of the intermediate state in quantum cutting.

■ CONCLUSIONS

In summary, a combination of NC and thin-film synthesis, VTPL and TRPL spectroscopies, and calculations of exciton-binding energies has been used to elucidate the impact of RE^{3+} doping on the electronic structures and photophysics of all-inorganic $CsPb(Cl_{1-x}Br_x)_3$ ($0 \leq x \leq 1$) lead-halide perovskites. The data show that RE^{3+} doping universally generates a new shallow defect state ca. 50 meV inside the perovskite band gap, regardless of the specific RE^{3+} dopant. Although most easily observed at low temperatures as the origin of a distinct PL band, this defect state is still influential at room temperature, leading to elongated PL decay times relative to the analogous undoped perovskite compositions. The appearance of this NBE PL even when doping with spectroscopically innocent RE^{3+} ions suggests that it originates in the charge-compensating defects that accompany substitution of Pb^{2+} by RE^{3+}. Overall, these findings advance our general fundamental understanding of defects in lead-halide perovskites by demonstrating that controlled aliovalent RE^{3+} doping can be used to reproducibly tune the concentrations of well-behaved shallow defects, with potential ramifications for understanding and controlling the physical properties of metal-halide perovskites in various photovoltaic, electronic, and photonic technologies.

■ ASSOCIATED CONTENT

Supporting Information

The Supporting Information is available free of charge at https://pubs.acs.org/doi/10.1021/acs.chemmater.2c00132.

Extra experimental details and data including surface treatment, fitting analysis, TRPL, MCPL, and VT absorption and PL (PDF)

■ AUTHOR INFORMATION

Corresponding Author

Daniel R. Gamelin – *Department of Chemistry, University of Washington, Seattle, Washington 98195, United States;* orcid.org/0000-0003-2888-9916; Email: gamelin@uw.edu

Authors

Tyler J. Milstein – *Department of Chemistry, University of Washington, Seattle, Washington 98195, United States;* orcid.org/0000-0002-1517-2222

Joo Yeon D. Roh – *Department of Chemistry, University of Washington, Seattle, Washington 98195, United States;* orcid.org/0000-0001-9801-3069

Laura M. Jacoby – *Department of Chemistry, University of Washington, Seattle, Washington 98195, United States;* orcid.org/0000-0002-9308-7162

Matthew J. Crane – *Department of Chemistry, University of Washington, Seattle, Washington 98195, United States;* Present Address: Chemical and Biological Engineering Department, 1613 Illinois St., Colorado School of Mines, Golden, CO 80401, United States; orcid.org/0000-0001-8461-4808

David E. Sommer – *Department of Physics, University of Washington, Seattle, Washington 98195, United States*

Scott T. Dunham – *Department of Electrical and Computer Engineering, University of Washington, Seattle, Washington 98195, United States*

Complete contact information is available at: https://pubs.acs.org/10.1021/acs.chemmater.2c00132

Notes

The authors declare no competing financial interest.

■ ACKNOWLEDGMENTS

This work was primarily supported by the U.S. National Science Foundation through the University of Washington Molecular Engineering Materials Center, a Materials Research Science and Engineering Center (DMR-1719797 to D.R.G. and S.T.D.). Additional support from the U.S. National Science Foundation (DMR-1807394 to D.R.G.) is gratefully acknowledged. The authors thank the Research Corporation for Science Advancement (RCSA) for supporting this research via a 2021 Cottrell Fellowships Award (award #27993) to D.R.G. in support of M.J.C. Part of this work was conducted at the Molecular Analysis Facility, a National Nanotechnology Coordinated Infrastructure (NNCI) site at the University of Washington, which is supported in part by funds from the National Science Foundation (awards NNCI-2025489 and NNCI-1542101), the Molecular Engineering & Sciences Institute, and the Clean Energy Institute. Dr. Samantha Young is acknowledged for acquiring XRD data. Dr. Ellen Lavoie and Atch Gopalan are acknowledged for acquiring TEM images.

■ REFERENCES

(1) Jena, A. K.; Kulkarni, A.; Sanehira, Y.; Ikegami, M.; Miyasaka, T. Stabilization of α-$CsPbI_3$ in Ambient Room Temperature Conditions by Incorporating Eu into $CsPbI_3$. *Chem. Mater.* **2018**, *30*, 6668–6674.

(2) Shi, J.; Li, F.; Yuan, J.; Ling, X.; Zhou, S.; Qian, Y.; Ma, W. Efficient and stable $CsPbI_3$ perovskite quantum dots enabled by in situ ytterbium doping for photovoltaic applications. *J. Mater. Chem. A.* **2019**, *7*, 20936–20944.

(3) Duan, J.; Zhao, Y.; Yang, X.; Wang, Y.; He, B.; Tang, Q. Lanthanide Ions Doped CsPbBr3 Halides for HTM-Free 10.14%-Efficiency Inorganic Perovskite Solar Cell with an Ultrahigh Open-Circuit Voltage of 1.594 V. *Adv. Energy Mater.* **2018**, *8*, 1802346.

(4) Liu, Y.; Pan, G.; Wang, R.; Shao, H.; Wang, H.; Xu, W.; Cui, H.; Song, H. Considerably enhanced exciton emission of $CsPbCl_3$ perovskite quantum dots by the introduction of potassium and lanthanide ions. *Nanoscale* **2018**, *10*, 14067–14072.

(5) Yao, J.-S.; Ge, J.; Han, B.-N.; Wang, K.-H.; Yao, H.-B.; Yu, H.-L.; Li, J.-H.; Zhu, B.-S.; Song, J.-Z.; Chen, C.; Zhang, Q.; Zeng, H.-B.; Luo, Y.; Yu, S.-H. Ce^{3+}-Doping to Modulate Photoluminescence Kinetics for Efficient $CsPbBr_3$ Nanocrystals Based Light-Emitting Diodes. *J. Am. Chem. Soc.* **2018**, *140*, 3626–3634.

(6) Yin, J.; Ahmed, G. H.; Bakr, O. M.; Brédas, J.-L.; Mohammed, O. F. Unlocking the Effect of Trivalent Metal Doping in All-Inorganic $CsPbBr_3$ Perovskite. *ACS Energy Lett.* **2019**, *4*, 789−795.
(7) Guvenc, C. M.; Yalcinkaya, Y.; Ozen, S.; Sahin, H.; Demir, M. M. Gd^{3+}-Doped α-$CsPbI_3$ Nanocrystals with Better Phase Stability and Optical Properties. *J. Phys. Chem. C* **2019**, *123*, 24865−24872.
(8) Pan, G.; Bai, X.; Yang, D.; Chen, X.; Jing, P.; Qu, S.; Zhang, L.; Zhou, D.; Zhu, J.; Xu, W.; Dong, B.; Song, H. Doping Lanthanide into Perovskite Nanocrystals: Highly Improved and Expanded Optical Properties. *Nano Lett.* **2017**, *17*, 8005−8011.
(9) Mir, W. J.; Mahor, Y.; Lohar, A.; Jagadeeswararao, M.; Das, S.; Mahamuni, S.; Nag, A. Postsynthesis Doping of Mn and Yb into $CsPbX_3$ (X = Cl, Br, or I) Perovskite Nanocrystals for Down-conversion Emission. *Chem. Mater.* **2018**, *30*, 8170−8178.
(10) Zhou, D.; Sun, R.; Xu, W.; Ding, N.; Li, D.; Chen, X.; Pan, G.; Bai, X.; Song, H. Impact of Host Composition, Codoping, or Tridoping on Quantum-Cutting Emission of Ytterbium in Halide Perovskite Quantum Dots and Solar Cell Applications. *Nano Lett.* **2019**, *19*, 6904−6913.
(11) Zhou, D.; Liu, D.; Pan, G.; Chen, X.; Li, D.; Xu, W.; Bai, X.; Song, H. Cerium and Ytterbium Codoped Halide Perovskite Quantum Dots: A Novel and Efficient Downconverter for Improving the Performance of Silicon Solar Cells. *Adv. Mater.* **2017**, *29*, 1704149.
(12) Kroupa, D. M.; Roh, J. Y.; Milstein, T. J.; Creutz, S. E.; Gamelin, D. R. Quantum-Cutting Ytterbium-Doped $CsPb(Cl_{1-x}Br_x)_3$ Perovskite Thin Films with Photoluminescence Quantum Yields over 190%. *ACS Energy Lett.* **2018**, *3*, 2390−2395.
(13) Milstein, T. J.; Kroupa, D. M.; Gamelin, D. R. Picosecond Quantum Cutting Generates Photoluminescence Quantum Yields Over 100% in Ytterbium-Doped $CsPbCl_3$ Nanocrystals. *Nano Lett.* **2018**, *18*, 3792−3799.
(14) Zhang, X.; Zhang, Y.; Zhang, X.; Yin, W.; Wang, Y.; Wang, H.; Lu, M.; Li, Z.; Gu, Z.; Yu, W. W. Yb^{3+} and Yb^{3+}/Er^{3+} doping for near-infrared emission and improved stability of $CsPbCl_3$ nanocrystals. *J. Mater. Chem. C* **2018**, *6*, 10101−10105.
(15) Cohen, T. A.; Milstein, T. J.; Kroupa, D. M.; MacKenzie, J. D.; Luscombe, C. K.; Gamelin, D. R. Quantum-cutting Yb^{3+}-doped perovskite nanocrystals for monolithic bilayer luminescent solar concentrators. *J. Mater. Chem. A.* **2019**, *7*, 9279−9288.
(16) Crane, M. J.; Kroupa, D. M.; Roh, J. Y.; Anderson, R. T.; Smith, M. D.; Gamelin, D. R. Single-Source Vapor Deposition of Quantum-Cutting Yb^{3+}:$CsPb(Cl_{1-x}Br_x)_3$ and Other Complex Metal-Halide Perovskites. *ACS Appl. Energy Mater.* **2019**, *2*, 4560−4565.
(17) Erickson, C. S.; Crane, M. J.; Milstein, T. J.; Gamelin, D. R. Photoluminescence Saturation in Quantum-Cutting Yb^{3+}-Doped $CsPb(Cl_{1-x}Br_x)_3$ Perovskite Nanocrystals: Implications for Solar Downconversion. *J. Phys. Chem. C* **2019**, *123*, 12474−12484.
(18) Luo, X.; Ding, T.; Liu, X.; Liu, Y.; Wu, K. Quantum-Cutting Luminescent Solar Concentrators Using Ytterbium-Doped Perovskite Nanocrystals. *Nano Lett.* **2019**, *19*, 338−341.
(19) Milstein, T. J.; Kluherz, K. T.; Kroupa, D. M.; Erickson, C. S.; De Yoreo, J. J.; Gamelin, D. R. Anion Exchange and the Quantum-Cutting Energy Threshold in Ytterbium-Doped $CsPb(Cl_{1-x}Br_x)_3$ Perovskite Nanocrystals. *Nano Lett.* **2019**, *19*, 1931−1937.
(20) Cai, T.; Wang, J.; Li, W.; Hills-Kimball, K.; Yang, H.; Nagaoka, Y.; Yuan, Y.; Zia, R.; Chen, O. Mn^{2+}/Yb^{3+} Codoped $CsPbCl_3$ Perovskite Nanocrystals with Triple-Wavelength Emission for Luminescent Solar Concentrators. *Adv. Sci.* **2020**, *7*, 2001317.
(21) Ding, N.; Xu, W.; Zhou, D.; Ji, Y.; Wang, Y.; Sun, R.; Bai, X.; Zhou, J.; Song, H. Extremely efficient quantum-cutting Cr^{3+}, Ce^{3+}, Yb^{3+} tridoped perovskite quantum dots for highly enhancing the ultraviolet response of Silicon photodetectors with external quantum efficiency exceeding 70. *Nano Energy* **2020**, *78*, 105278.
(22) Ishii, A.; Miyasaka, T. Quantum cutting-induced near-infrared luminescence of Yb^{3+} and Er^{3+} in a layer structured perovskite film. *J. Chem. Phys.* **2020**, *153*, 194704.
(23) Roh, J. Y. D.; Smith, M. D.; Crane, M. J.; Biner, D.; Milstein, T. J.; Krämer, K. W.; Gamelin, D. R. Yb^{3+} speciation and energy-transfer dynamics in quantum-cutting Yb^{3+}-doped $CsPbCl_3$ perovskite nanocrystals and single crystals. *Phys. Rev. Mater.* **2020**, *4*, 105405.
(24) Zeng, M.; Artizzu, F.; Liu, J.; Singh, S.; Locardi, F.; Mara, D.; Hens, Z.; Van Deun, R. Boosting the Er^{3+} 1.5 μm Luminescence in $CsPbCl_3$ Perovskite Nanocrystals for Photonic Devices Operating at Telecommunication Wavelengths. *ACS Appl. Nano Mater.* **2020**, *3*, 4699−4707.
(25) Zhu, Y.; Pan, G.; Shao, L.; Yang, G.; Xu, X.; Zhao, J.; Mao, Y. Effective infrared emission of erbium ions doped inorganic lead halide perovskite quantum dots by sensitization of ytterbium ions. *J. Alloys Compd.* **2020**, *835*, 155390.
(26) Huang, H.; Li, R.; Jin, S.; Li, Z.; Huang, P.; Hong, J.; Du, S.; Zheng, W.; Chen, X.; Chen, D. Ytterbium-Doped $CsPbCl_3$ Quantum Cutters for Near-Infrared Light-Emitting Diodes. *ACS Appl. Mater. Interfaces* **2021**, *13*, 34561−34571.
(27) Xu, K.; Chen, D.; Huang, D.; Zhu, H. Thermally stable emission from Yb^{3+}-doped $CsPbCl_3$ nanocrystals. *J. Lumin.* **2021**, *240*, 118464.
(28) Chang, W. J.; Irgen-Gioro, S.; Padgaonkar, S.; López-Arteaga, R.; Weiss, E. A. Photoredox-Mediated Sensitization of Lanthanide Dopants by Perovskite Nanocrystals. *J. Phys. Chem. C* **2021**, *125*, 25634−25642.
(29) Creutz, S. E.; Crites, E. N.; De Siena, M. C.; Gamelin, D. R. Anion Exchange in Cesium Lead Halide Perovskite Nanocrystals and Thin Films Using Trimethylsilyl Halide Reagents. *Chem. Mater.* **2018**, *30*, 4887−4891.
(30) Creutz, S. E.; Crites, E. N.; De Siena, M. C.; Gamelin, D. R. Colloidal nanocrystals of lead-free double-perovskite (elpasolite) semiconductors: synthesis and anion exchange to access new materials. *Nano Lett.* **2018**, *18*, 1118−1123.
(31) Kroupa, D. M.; Crane, M. J.; Gamelin, D. R. Single-source flash sublimation of metal-halide semiconductors. *Proc. SPIE* **2019**, *11084*, 110840J.
(32) Sommer, D. E.; Gamelin, D. R.; Dunham, S. T. Defect formation in Yb-doped $CsPbCl_3$ from first principles with implications for quantum cutting. *Phys. Rev. Mater.* **2022**, *6*, 025404.
(33) Protesescu, L.; Yakunin, S.; Bodnarchuk, M. I.; Krieg, F.; Caputo, R.; Hendon, C. H.; Yang, R. X.; Walsh, A.; Kovalenko, M. V. Nanocrystals of Cesium Lead Halide Perovskites ($CsPbX_3$, X = Cl, Br, and I): Novel Optoelectronic Materials Showing Bright Emission with Wide Color Gamut. *Nano Lett.* **2015**, *15*, 3692−3696.
(34) Linaburg, M. R.; McClure, E. T.; Majher, J. D.; Woodward, P. M. $Cs_{1-x}Rb_xPbCl_3$ and $Cs_{1-x}Rb_xPbBr_3$ Solid Solutions: Understanding Octahedral Tilting in Lead Halide Perovskites. *Chem. Mater.* **2017**, *29*, 3507−3514.
(35) Quarati, F. G. A.; Dorenbos, P.; van der Biezen, J.; Owens, A.; Selle, M.; Parthier, L.; Schotanus, P. Scintillation and detection characteristics of high-sensitivity $CeBr_3$ gamma-ray spectrometers. *Nucl. Instrum. Methods Phys. Res., Sect. A* **2013**, *729*, 596−604.
(36) Steele, J. A.; Puech, P.; Monserrat, B.; Wu, B.; Yang, R. X.; Kirchartz, T.; Yuan, H.; Fleury, G.; Giovanni, D.; Fron, E.; Keshavarz, M.; Debroye, E.; Zhou, G.; Sum, T. C.; Walsh, A.; Hofkens, J.; Roeffaers, M. B. J. Role of Electron−Phonon Coupling in the Thermal Evolution of Bulk Rashba-Like Spin-Split Lead Halide Perovskites Exhibiting Dual-Band Photoluminescence. *ACS Energy Lett.* **2019**, *4*, 2205−2212.
(37) Dendebera, M.; Chornodolskyy, Y.; Gamernyk, R.; Antonyak, O.; Pashuk, I.; Myagkota, S.; Gnilitskyi, I.; Pankratov, V.; Vistovskyy, V.; Mykhaylyk, V.; Grinberg, M.; Voloshinovskii, A. Time resolved luminescence spectroscopy of $CsPbBr_3$ single crystal. *J. Lumin.* **2020**, *225*, 117346.
(38) Ryu, H.; Park, D. Y.; McCall, K. M.; Byun, H. R.; Lee, Y.; Kim, T. J.; Jeong, M. S.; Kim, J.; Kanatzidis, M. G.; Jang, J. I. Static Rashba Effect by Surface Reconstruction and Photon Recycling in the Dynamic Indirect Gap of $APbBr_3$ (A = Cs, CH_3NH_3) Single Crystals. *J. Am. Chem. Soc.* **2020**, *142*, 21059−21067.
(39) Haken, H. Zur Quantentheorie des Mehrelektronensystems im schwingenden Gitter. I. *Z. Phys.* **1956**, *146*, 527−554.

https://doi.org/10.1021/acs.chemmater.2c00132
Chem. Mater. XXXX, XXX, XXX−XXX

(40) Haken, H. Die Theorie des Exzitons im festen Körper. *Fortschr. Phys.* **1958**, *6*, 271−334.
(41) Feynman, R. P. Slow Electrons in a Polar Crystal. *Phys. Rev.* **1955**, *97*, 660−665.
(42) Filip, M. R.; Haber, J. B.; Neaton, J. B. Phonon Screening of Excitons in Semiconductors: Halide Perovskites and Beyond. *Phys. Rev. Lett.* **2021**, *127*, 067401.
(43) Zhang, Q.; Su, R.; Liu, X.; Xing, J.; Sum, T. C.; Xiong, Q. High-Quality Whispering-Gallery-Mode Lasing from Cesium Lead Halide Perovskite Nanoplatelets. *Adv. Funct. Mater.* **2016**, *26*, 6238−6245.
(44) Yang, Z.; Surrente, A.; Galkowski, K.; Miyata, A.; Portugall, O.; Sutton, R. J.; Haghighirad, A. A.; Snaith, H. J.; Maude, D. K.; Plochocka, P.; Nicholas, R. J. Impact of the Halide Cage on the Electronic Properties of Fully Inorganic Cesium Lead Halide Perovskites. *ACS Energy Lett.* **2017**, *2*, 1621−1627.
(45) Baranowski, M.; Plochocka, P.; Su, R.; Legrand, L.; Barisien, T.; Bernardot, F.; Xiong, Q.; Testelin, C.; Chamarro, M. Exciton binding energy and effective mass of $CsPbCl_3$: a magneto-optical study. *Photon. Res.* **2020**, *8*, A50−A55.
(46) Lao, X.; Yang, Z.; Su, Z.; Wang, Z.; Ye, H.; Wang, M.; Yao, X.; Xu, S. Luminescence and thermal behaviors of free and trapped excitons in cesium lead halide perovskite nanosheets. *Nanoscale* **2018**, *10*, 9949−9956.
(47) Nikl, M.; Nitsch, K.; Mihóková, E.; Polák, K.; Fabeni, P.; Pazzi, G. P.; Gurioli, M.; Santucci, S.; Phani, R.; Scacco, A.; Somma, F. Luminescence of $CsPbBr_3$-like quantum dots in CsBr single crystals. *Phys. E* **1999**, *4*, 323−331.
(48) Han, Q.; Wu, W.; Liu, W.; Yang, Q.; Yang, Y. Temperature-dependent photoluminescence of $CsPbX_3$ nanocrystal films. *J. Lumin.* **2018**, *198*, 350−356.
(49) Li, X.; Duan, S.; Liu, H.; Chen, G.; Luo, Y.; Ågren, H. Mechanism for the Extremely Efficient Sensitization of Yb^{3+} Luminescence in $CsPbCl_3$ Nanocrystals. *J. Phys. Chem. Lett.* **2019**, *10*, 487−492.
(50) Manchon, A.; Koo, H. C.; Nitta, J.; Frolov, S. M.; Duine, R. A. New perspectives for Rashba spin−orbit coupling. *Nat. Mater.* **2015**, *14*, 871−882.
(51) Isarov, M.; Tan, L. Z.; Bodnarchuk, M. I.; Kovalenko, M. V.; Rappe, A. M.; Lifshitz, E. Rashba Effect in a Single Colloidal $CsPbBr_3$ Perovskite Nanocrystal Detected by Magneto-Optical Measurements. *Nano Lett.* **2017**, *17*, 5020−5026.

https://doi.org/10.1021/acs.chemmater.2c00132
Chem. Mater. XXXX, XXX, XXX−XXX